frontiers in Earth Science

ORIGINAL RESEARCH
published: 26 August 2021
doi: 10.3389/feart.2021.715278

Variation of Organic Pore Structure With Maceral Types in the Longmaxi Shale, Sichuan Basin

Qian Pang[1,2,3], *Guang Hu*[2,3]*, *Chaowei Hu*[2,3] *and Cong Zhang*[1]

[1]The Key Laboratory of Unconventional Petroleum Geology, CGS, Beijing, China, [2]State Key Laboratory of Oil and Gas Geology and Exploitation, Southwest Petroleum University, Chengdu, China, [3]Carbonate Sedimentology, PetroChina Key Laboratory of Carbonate Reservoir, Southwest Petroleum University, Chengdu, China

Organic matter (OM), composed of various macerals, has a strong influence on the enrichment of shale gas. Nevertheless, the connection between OM-hosted pore structure and maceral type is not yet fully understood because of the difficulty to identify the maceral types by traditional scanning electron microscope (SEM). Using a combination of the reflected light microscopy, focused ion beam SEM (FIB-SEM), and Raman spectrum, three maceral types, including alginite, graptolite, and solid bitumen, are identified in the Longmaxi Shale of the Sichuan Basin. The alginate is characterized by the linear arrangement of OM-hosted pores due to the inherited biological structure of benthic algae. Pores in the structureless solid bitumen are randomly distributed with the highest abundance. The graptolite containing pore rarely is unfavorable for the pore generation but can be a good proxy for thermal maturity. Variation in thermal maturity levels accounts for the change of total pore volume in a given marcel type in the Longmaxi Shale obtained from different shale gas fields.

Keywords: organic matter pores, maceral, Raman spectroscopy, longmaxi formation, Sichuan Basin

OPEN ACCESS

Edited by:
Feng Yang,
China University of Geosciences Wuhan, China

Reviewed by:
Lei Chen,
China University of Petroleum (Huadong), China
Kun Jiao,
Chengdu University of Technology, China

***Correspondence:**
Guang Hu
guanghu1198119@163.commailto: guanghu1198119@163.com

Specialty section:
This article was submitted to Economic Geology, a section of the journal Frontiers in Earth Science

Received: *26 May 2021*
Accepted: *22 July 2021*
Published: *26 August 2021*

Citation:
Pang Q, Hu G, Hu C and Zhang C (2021) Variation of Organic Pore Structure With Maceral Types in the Longmaxi Shale, Sichuan Basin. Front. Earth Sci. 9:715278. doi: 10.3389/feart.2021.715278

INTRODUCTION

Shale is a type of unconventional reservoir with micro- and nano-pores as the storage spaces (Zou et al., 2020, 2017). Organic matter (OM) pores are the most important storage spaces in shale reservoirs (Loucks et al., 2009; Jiao et al., 2014; Liu et al., 2020a,2020b). Microscopic OM pores have already been substantially studied (e.g., Loucks et al., 2009; Fishman et al., 2012; Mastalerz et al., 2013; Chen et al., 2015; Löhr et al., 2015; Ko et al., 2018). Many researchers point out that the OM contents, types, and distributions strongly affect the shale reservoir quality (Wang et al., 2016; Zhu et al., 2019).

However, the relationship between different macerals and their OM pores is not clear on the micro/nano-scale since it is such difficult to catch the micro/nano-pores in the macerals by using an optical measurement (Hakimi et al., 2012; Liu et al., 2017; Cardott et al., 2018; Guo et al., 2018). Some tentative studies have been carried out recently through a kind of combined multiple observation systems. Hackley et al. (2017) employed the integrated correlative light and electron microscopy (iCLEM) to study different OM types. Liu et al. (2017) compared the OM characteristics under reflected light and scanning electron microscope. Guan et al. (2019) investigated the OM characteristics changes under a scanning electron microscope and atomic force microscope. However, the difficulty of identifying and analyzing pores in different macerals over different

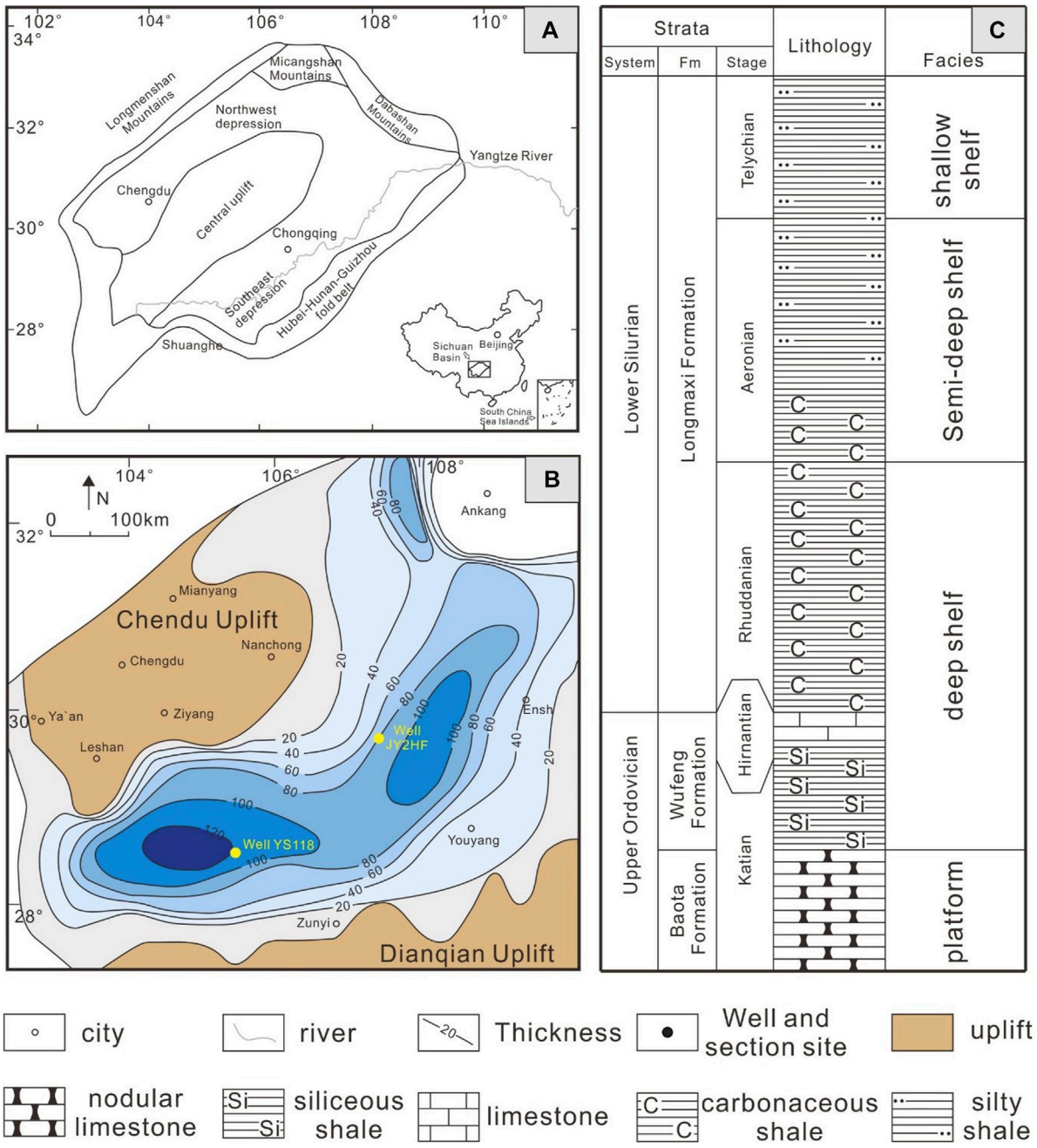

FIGURE 1 | (A) The geographical location of the study area, **(B)** Early Silurian paleogeographic map of the study area (modified from Wang et al., 2015), **(C)** Stratigraphic column.

experiments hinders the further study of the characteristics of pores in different macerals and their origin.

In addition, the differences between pores in different macerals in the Longmaxi Formation also need to be explained. It is well-known that Raman spectroscopy can characterize the structural orders of carbonaceous materials *in situ* micro areas. Then, several Raman parameters have been used to characterize structural orderings (Jehlička et al., 2003; Guedes et al., 2012) to explore the functional groups (Morga et al., 2011) and to detect the marcel structures (Guedes et al., 2012). Many scholars have focused on the relationship between the Raman parameters of coal and source rock thermal maturity (e.g., Zhou et al., 2014; Liu et al., 2018). Some scholars have also conducted Raman spectroscopy analyses on different macerals and different types of organisms in shale to obtain structural information and hydrocarbon generation capacity

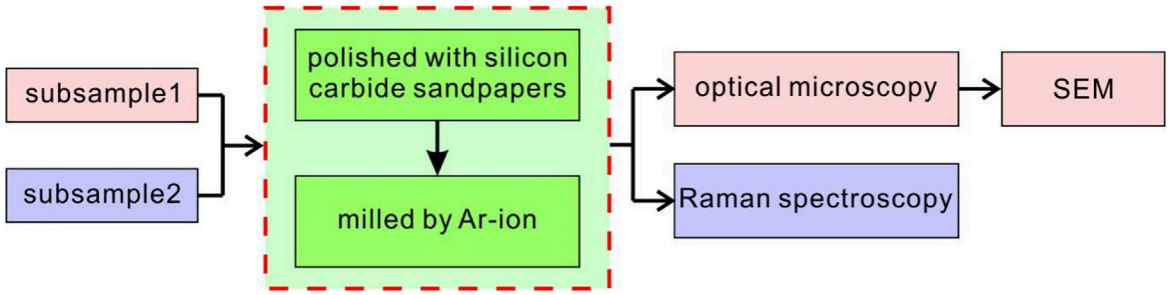

FIGURE 2 | Flow chart of experimental analysis, which mainly includes the immersion oil reflected light observation and Raman spectrum testing. Subsample 1 was tested by immersion oil reflected light and SEM, and subsample 2 was tested by Raman spectroscopy.

(Guedes et al., 2010; Bao et al., 2012; Mumm et al., 2016; Ferralis et al., 2016; Shang et al., 2018).

In this study, two Lower Silurian Longmaxi shale samples from two shale gas fields of Sichuan were collected and analyzed. The main objective is to 1) obtain the organic petrology characteristics and pore structures of different macerals under the microscope reflected light, 2) analyze the chemical components of maceral by Raman spectroscopy, and 3) research the controlling pore structures factors of the different macerals.

GEOLOGICAL BACKGROUND

The two shale samples were selected from Well YS118 and JY2HF, which are located in the Changning-Weiyuan area and the Fuling area with a burial depth of 2,231.0 m and 2,570.3 m, respectively. These two areas are both located in the main shale gas production areas in the Sichuan basin (**Figure 1**). OM types in the Longmaxi Formation are classified as type II kerogen (Tenger et al., 2017). The main maceral types of the Longmaxi Formation include alginite, solid bitumen, and graptolite (Dai et al., 2014; Liang et al., 2014; Ma et al., 2016). The thermal maturity is at the high-over maturity stage (Zou et al., 2020; Hu et al., 2017; Chen et al., 2019).

MATERIALS AND METHODS

Two subsamples (subsample 1 and subsample 2) of each sample (jy2 HF and ys118) were cut parallel to the bedding with a saw blade at 10 mm intervals, and every subsample was ground into $1 \times 1 \times 1\ cm^3$ cubes (**Figure 2**). Then, they were polished by silicon carbide sandpapers of 300, 600, 1000, and 2000 mesh in succession. Ultimately, they were polished for about 8 h to produce a high-quality cross-section by argon ions with a Leica EM TIC 3X mill using an accelerating voltage of 8 kV and a current of 2.8 mA.

Maceral Observation

Subsample 1 was observed under the microscope reflected light in the oil-immersed environment (the magnification of the objective lens was 50 times) (**Figure 2**). Different typical macerals of subsample 1 were identified under reflected light, including the three macerals of alginite, solid bitumen, and graptolite (**Figure 3**). Detailed maceral identification and analysis methods have been shown by Hu et al. (2020).

SEM and OM Pores Statistics

The imaging was performed at an accelerating voltage of 2 kV with a working distance of 10 mm. To obtain statistically significant and representative areal porosity, twenty SEM images are photographed at random. Pores are visualized in the SEM images, characterized by the gray value pattern of a bright rim and a dark pore body. This feature makes it possible to identify pores with some automatic methods, such as Image-Pro Plus. The pore parameters are analyzed in this software. The form factor (*ff*) is a descriptor of the shape of features and reflects the circularity and roughness of pore edges. It has a maximum value of 1.0 (for a circle) or 0.785 (for a square). The complexity of the pore boundary increases with decreasing form factors. The form factor is defined as $ff = 4 \cdot \pi \cdot S/C^2$, where S is pore area and C is pore perimeter (Jiao et al., 2014).

Raman Spectroscopy

Subsample 2 was utilized to analyze the Raman spectroscopy (**Figure 2**). During the test, the identified maceral was photographed first, and then different maceral types (the identification properties are shown in *Maceral* section and *Pore Characteristics* section) were tested by the Raman spectroscopy. The Raman spectroscopy analysis was carried out in the laboratory of the college of chemical engineering and technology, Southwest Petroleum University. The instrument (MicroTEQ-R1) was made by an American Oceanoptics company. The wavelength of the excitation light source is 785 nm. Raman displacement ranges from 200 cm^{-1} to 2000 cm^{-1} with a resolution of 4 cm^{-1}. The laser spot size is about 2 μm and the magnification of the microscope objective is 40 times.

RESULTS

Maceral

Alginite, solid bitumen, and graptolite are observed under immersion oil reflected light (**Figure 3**). **Figure 4** shows a

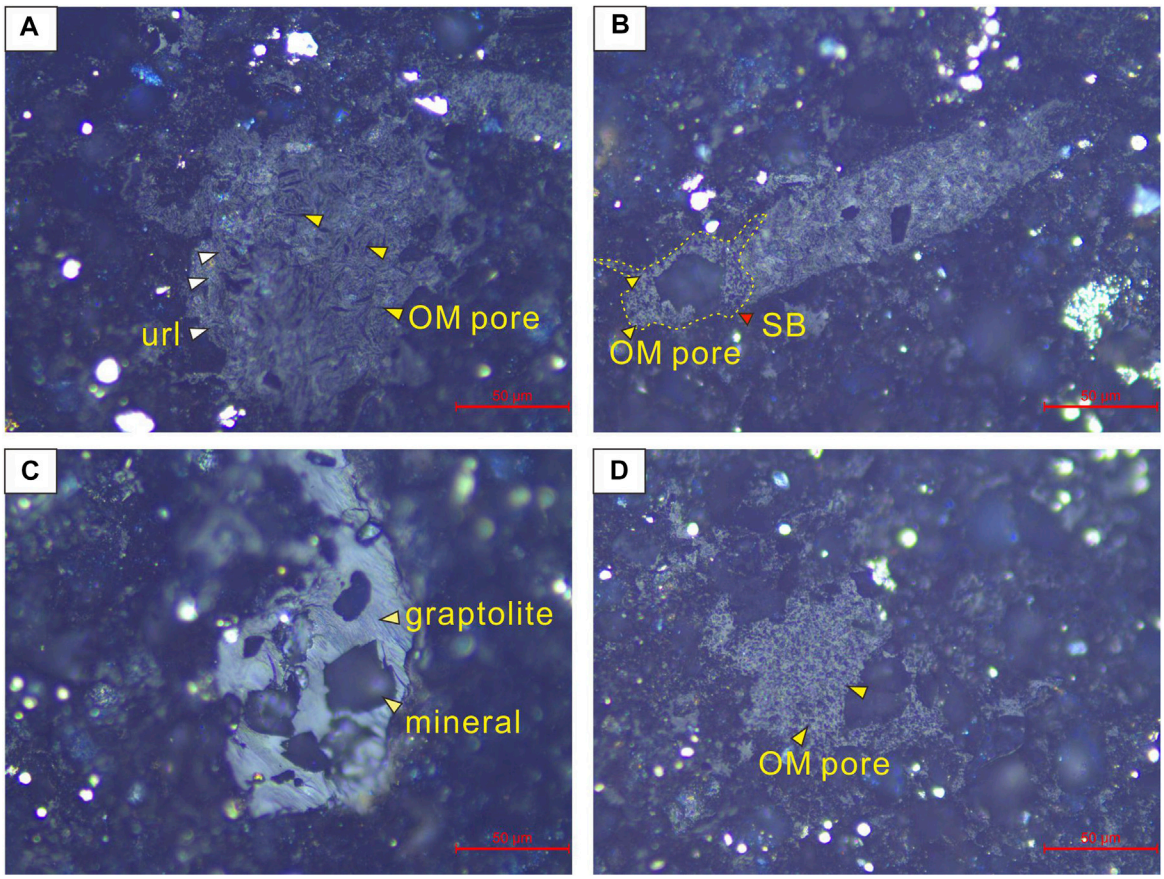

FIGURE 3 | Maceral optics and structure characteristics, argon ion polished section, immersion oil objective. **(A)** Alginite, with an ultralaminae network structure and linear OM pores. **(B)** Alginite, noting that the alginite is gradually converted to solid bitumen. **(C)** Graptolite, the mineral particles cut through the graptolite surface (Hu et al., 2020). **(D)** Solid bitumen, with homogeneous organic rounded pores. url = "ultralaminae"; SB = "solid bitumen".

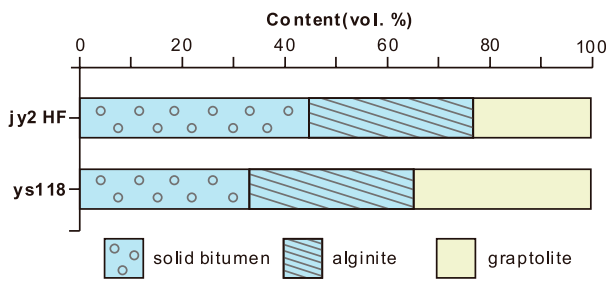

FIGURE 4 | The distribution of macerals in shale samples.

predominance of solid bitumen in the samples. The occurrence of graptolites and alginate is less than 50 vol% within the shales.

Both alginite and graptolite are comprised of granular, slablike, or irregular bands with sharp and distinct boundaries (**Figures 3A,B,C**). However, solid bitumen filling which exists among mineral grains is non-granular (**Figure 3D**). Alginite is easily distinguished due to its unique morphologies, consisting of ultralaminae network structures with a thickness of about 5 μm (**Figures 3A,B**). Commonly, no other biological structures exist in the solid bitumen except honeycomb OM pores (**Figure 3D**). The reflectance of graptolites is higher than those of alginite and solid bitumen (**Figure 3C**). Few OM pores are observed in graptolite, whereas plenty of OM pores are within alginite and solid bitumen. Also, the honeycomb OM pores are in the solid bitumen, and petal-like and linear pores are contained in the alginate (**Figure 3**).

Pore Characteristics

Based on the color differences between OM pores and OM, a large number of OM pores are identified for their blackish grey performances, and OM was grey in SEM (**Figure 5**). Under the SEM observations, alginate OM pores are comprised of elongated pores between lamellar and reticular structures, while the solid bitumen OM pores are evenly distributed in honeycomb shapes (**Figure 5**). The pore structure observed under SEM is similar to that under the reflected light microscopy (**Figure 3**).

Table 1 shows the result of quantitative pore structures of alginite and solid bitumen, including the parameters of areal porosity, mean pore size, and form factor. Alginite porosity and solid bitumen porosity in the jy2 HF sample have average values of 16.2 and 14.3%, respectively, while they are 11.7 and 10.5% in the

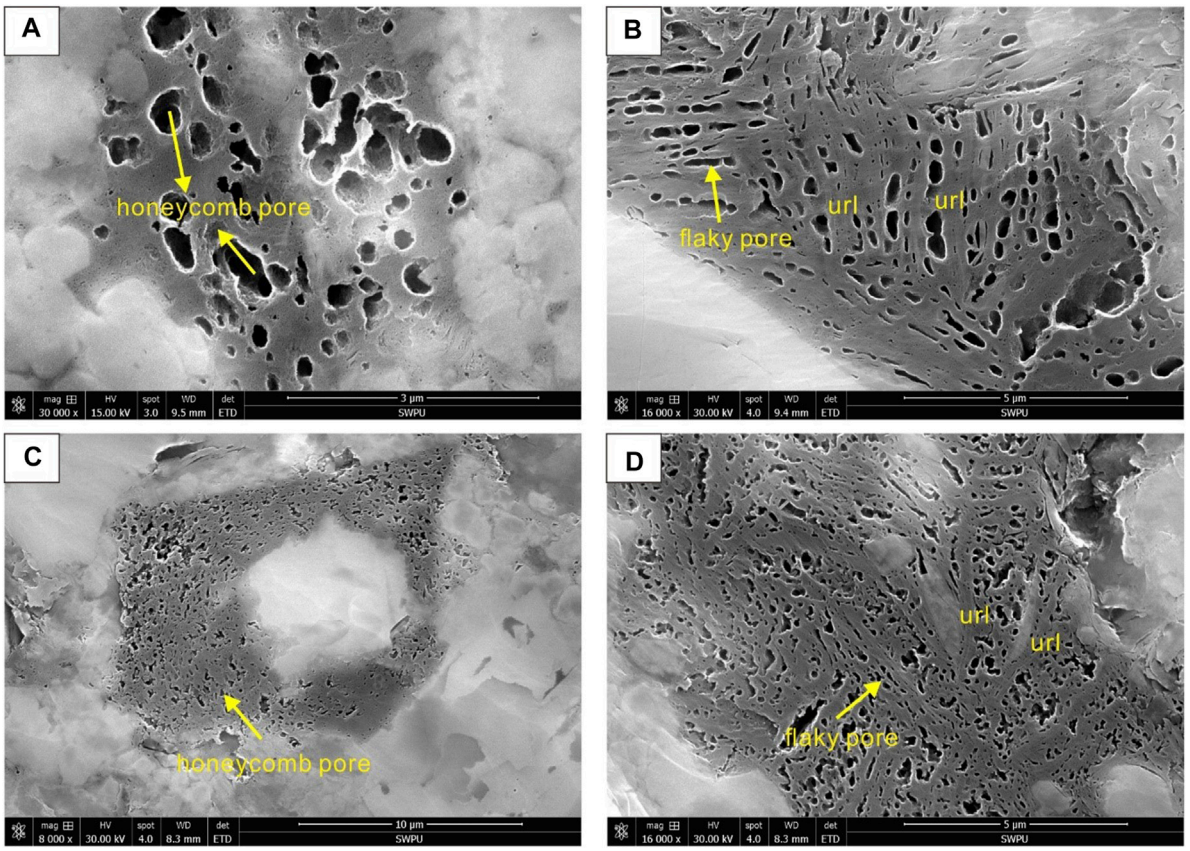

FIGURE 5 | OM pores in different macerals. **(A)** Solid bitumen, jy2 HF sample; **(B)** alginite, jy2 HF sample (Hu et al., 2020); **(C)** solid bitumen, ys118 sample; **(D)** alginite, ys118 sample.

TABLE 1 | OM pores Parameters in the Longmaxi Shale from the FE-SEM images.

Samples	TOC[a]	Marcel	Areal porosity (%)	Pore size (nm)	Form factor
jy2 HF	4.17	alginite	16.2	87.4	0.73
		solid bitumen	14.3	102.3	0.76
ys118	3.72	alginite	11.7	74.7	0.64
		solid bitumen	10.5	63.4	0.66

[a]*The TOC dates quote from Hu et al. (2020).*

ys118 sample, respectively. Pore sizes of alginite and solid bitumen in the jy2 HF sample have average values of 87.4 and 102.3 nm, whereas they are 74.7 and 63.4 nm in the ys118 sample, respectively. The form factors of alginite and solid bitumen in the jy2 sample HF have average values of 0.73 and 0.76, while they are 0.64 and 0.66 in the ys118 sample, respectively (**Table 1**). Generally, the OM pores of the jy2 HF sample have a larger areal porosity, pore size, and form factor than that of the ys118 sample.

Raman Characteristics

The alginite, solid bitumen, and graptolites all have the first-order Raman spectrum D band (~1,350 cm^{-1}) and G band (~1,595 cm^{-1}). The D band is caused by disordered structure or in-plane defects, while the G band is caused by the breathing of the aromatic ring in amorphous materials (Ferrari et al., 2000). In addition, other secondary bands probably contain structural information in the macerals except for the D and G bands (**Figure 6**). In this study, the curve fitting method is applied to decompose Raman spectroscopy (Hinrichs et al., 2014). Five secondary peaks are obtained by combining the four Lorentzian/Gaussian methods with D1, D2, D3, D4, and G bands at around 1,350 cm^{-1}, 1,540 cm^{-1}, 1,230 cm^{-1}, 1,185 cm^{-1}, and 1,595 cm^{-1}, respectively (**Figure 7**). D2 band is the vibration mode of the semicircular aromatic breathing ring. D3 band is aryl-alkyl ether and para-aromatics. D4 band is a hydrogen aromatic ring on C-H and C-C stretching vibration (Liu et al., 2018).

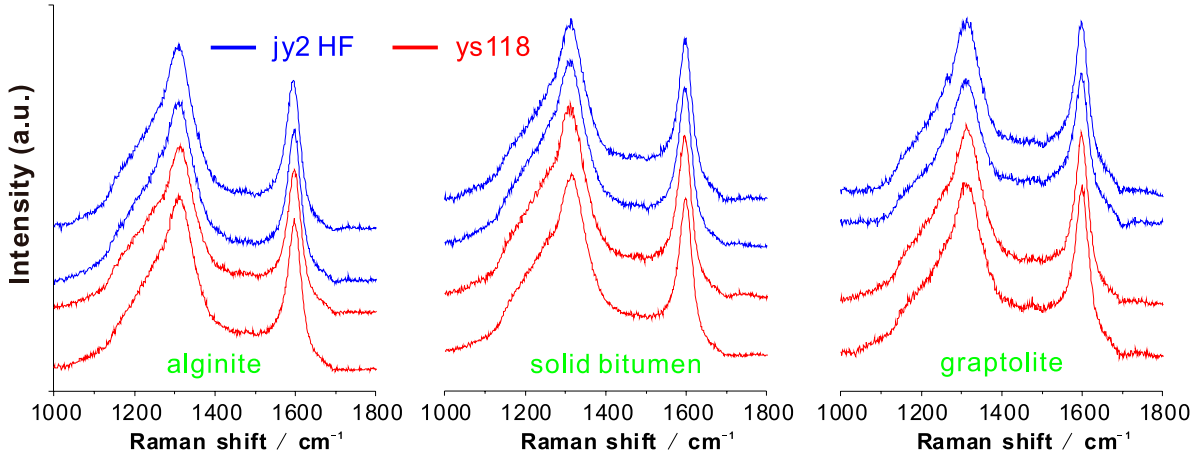

FIGURE 6 | Raman spectroscopy of alginite, solid bitumen, and graptolites in two samples, in which the blue line is the jy2 HF sample and the red line is the ys118 sample.

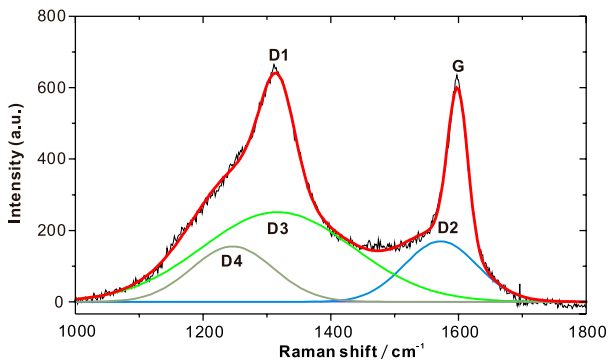

FIGURE 7 | Curve fitting of Raman spectrum for a representative sample.

To characterize the geochemical differences of three macerals, the following quantitative parameters are selected according to previous studies (Tenger et al., 2017; Kelemen et al., 2001; Sonibare et al., 2010), and these data are shown in **Table 2**:

1) Band separation of G and D1 (G-D);
2) Full half-peak width of D and G bands (FWHM-G);
3) Ratio of the full half-peak width of D to that of G bands (FWHM-D/G);
4) Intensity ratio of G to D band (ID/IG);
5) Area ratio of G to D band (AD/AG).

DISCUSSION

Possible Maceral and OM Pores Sources

The typical structure of alginate is the ultralaminae structure, which consists of the laminaes with the thickness of about 5 μm thick and the elongated pores between the laminaes (**Figures 3A,B**). Alginite is curved, elongated, or irregular plates (**Figures 3A,B**). Ultralaminae structures with elongated pores are also found in the Longmaxi Formation (Ma et al., 2016) and the Cambrian-Neogene amorphous kerogen (Largeau et al., 1990). Because their thin laminae range between 10 and 60 nm, these ultralaminae structures macerals are grouped into sapropel and derive from the accumulation of microalgae or cyanobacteria (Largeau et al., 1990; Pacton et al., 2006; Ma et al., 2016). However, the ultralaminae structures of the alginites found in this study are much thicker than microalgae. At the same time, the alveolar pores rather than enlarged pores within cyanobacteria indicate that alginite is not originated from cyanobacteria because alveolar pores are observed from cyanobacteria (Pacton et al., 2006). Eventually, we consider that the maceral might not be formed by microalgae or cyanobacteria.

Interestingly, macroscopic algal ultralaminae structures thickness is mostly a few microns in size (Tinn et al., 2015; Hu et al., 2020), which is the same as ultralaminae structures in **Figures 3A,B**. Further, in the Silurian strata, a large number of macro-benthic algae have been found, such as red algae (Zeng et al., 2015; Nie et al., 2018), green algae (Tinn et al., 2015), and other types of algae (Mastik and Tinn, 2017). In addition, Hu et al. (2020) found the red algae cysts through palynological analysis in the shale of the Silurian Longmaxi Formation, and these ultra-laminae structures were mainly related to the central axis and longitudinal filaments, presenting a long-axis type (Tinn et al., 2015; Hu et al., 2020). Therefore, ultra-laminae structures in the Longmaxi Formation are confirmed from the existence of macro-benthic algae. Alginite predominantly contains interlaminar pores and secondary bitumen pores. The areal porosity of alginite is the largest among these three maceral types (**Figure 5**; **Table 1**).

Solid bitumen stems from not only the transformation of alginite (**Figure 3B**) but also the degradation of crude oil (Misch et al., 2019). Then, it is filled in the spaces between minerals of the shale (**Figure 3C**). The secondary pores formed in solid bitumen

TABLE 2 | Raman structure parameters of three macerals for the two samples.

Samples	Maceral	Ro	G-D/cm^{-1}	FWHM-G/cm^{-1}	ID/IG	AD/AG	FWHM-D/G
jy2 HF	Alginite	2.48	288.29	76.57	1.26	3.65	2.90
			286.52	65.87	1.16	3.63	3.13
			288.28	68.86	1.16	3.51	3.03
			284.89	76.36	1.10	3.02	2.74
			290.54	67.50	1.10	3.48	3.16
			287.70	**71.03**	**1.16**	**3.46**	**2.99**
	Solid bitumen		282.25	69.91	1.06	3.22	3.05
			286.02	68.65	1.08	3.32	3.07
			286.40	69.41	1.07	3.24	3.03
			283.38	72.94	1.06	3.15	2.96
			286.40	67.22	1.07	3.53	3.14
			284.89	**69.63**	**1.07**	**3.29**	**3.05**
	Graptolite		285.00	84.18	1.07	2.81	2.62
			286.40	83.39	1.07	3.00	2.81
			286.40	81.79	1.04	2.78	2.69
			285.65	85.49	1.03	2.45	2.37
			286.40	87.31	0.98	2.24	2.29
			285.97	**84.43**	**1.04**	**2.66**	**2.56**
			286.19	***75.03***	***1.09***	***3.14***	***2.87***
ys118	Alginite	2.70	290.17	68.46	1.14	3.40	2.99
			286.40	68.41	1.12	3.62	3.22
			285.65	67.66	1.11	3.63	3.27
			288.28	68.39	1.13	3.67	3.26
			284.89	70.39	1.17	3.73	3.20
			287.08	**68.66**	**1.13**	**3.61**	**3.19**
	Solid bitumen		286.40	67.84	1.09	3.38	3.12
			284.25	66.57	1.10	3.59	3.28
			284.90	62.83	1.09	3.73	3.43
			284.89	66.68	1.14	3.73	3.27
			284.13	67.41	1.10	3.54	3.13
			284.91	**66.27**	**1.10**	**3.59**	**3.25**
	Graptolite		286.40	70.25	1.04	3.12	3.02
			282.86	69.01	1.04	3.29	3.17
			281.50	67.05	1.06	3.34	3.15
			284.13	68.65	1.00	3.18	3.17
			288.67	71.39	1.00	3.19	3.20
			284.71	**69.27**	**1.03**	**3.22**	**3.14**
			285.57	***68.07***	***1.09***	***3.48***	***3.19***

Note: Bold means the average values of macerals. Slant and bold represent the mean value of this parameter in the sample. Ro values are taken from Hu et al. (2020).

are uniform (**Figure 5**). The areal porosity and pore size were much poor compared to those of the alginite maceral (**Table 2**).

Graptolite has been debated in the literature whether there are a large number of pores (e.g., Ma et al., 2016; Luo et al., 2016, 2018). Almost no pore is ever found in graptolite of this study (**Figure 3**), although previous studies observed certain micrometer-sized fractures and spindle-shaped pores between cortical fibrils in the cortical of graptolite (Luo et al., 2016, 2018).

Macerals Difference in Terms of Raman Structure Parameters

Different optical characteristics and OM pores development in the macerals are attributed to their chemical structure (Jehlička et al., 2003; Bao et al., 2012). In what follows, Raman spectral parameters of the three macerals are discussed. **Table 2** and **Figure 7** exhibit the variation rules of different macerals in the two samples. The summary of the observations is as follows:

1) The mean AD/AG and the mean ID/IG values of graptolites are smaller than those of alginite and solid bitumen (**Table 2**; **Figures 8A–D**), which indicate more carbon content in the graptolites. The reason is that the AD/AG and ID/IG are a negative correlation with the size of a planar microcrystal and the carbon content (Tuinstra et al., 1970; Zhou et al., 2014; Bao et al., 2012; Mumm et al., 2016). Other results also support the conclusions. Firstly, the microscope reflected light observation indicating that the reflectivity of graptolites is significantly higher than those of alginite and solid bitumen (**Figure 3**), indicating the higher carbon content of graptolites. Secondly, the hard part of graptolite is almost comprised of chitin or multiple amino acids of hard protein, which are weak in hydrocarbon generation and are easily degraded (Luo et al., 2016). Lastly, the content of carbon elements in the graptolite was close to 100% by the energy spectrum of the Longmaxi Formation (Ma et al., 2015). In conclusion, the carbonization degree of graptolite is much stronger than those of alginite and

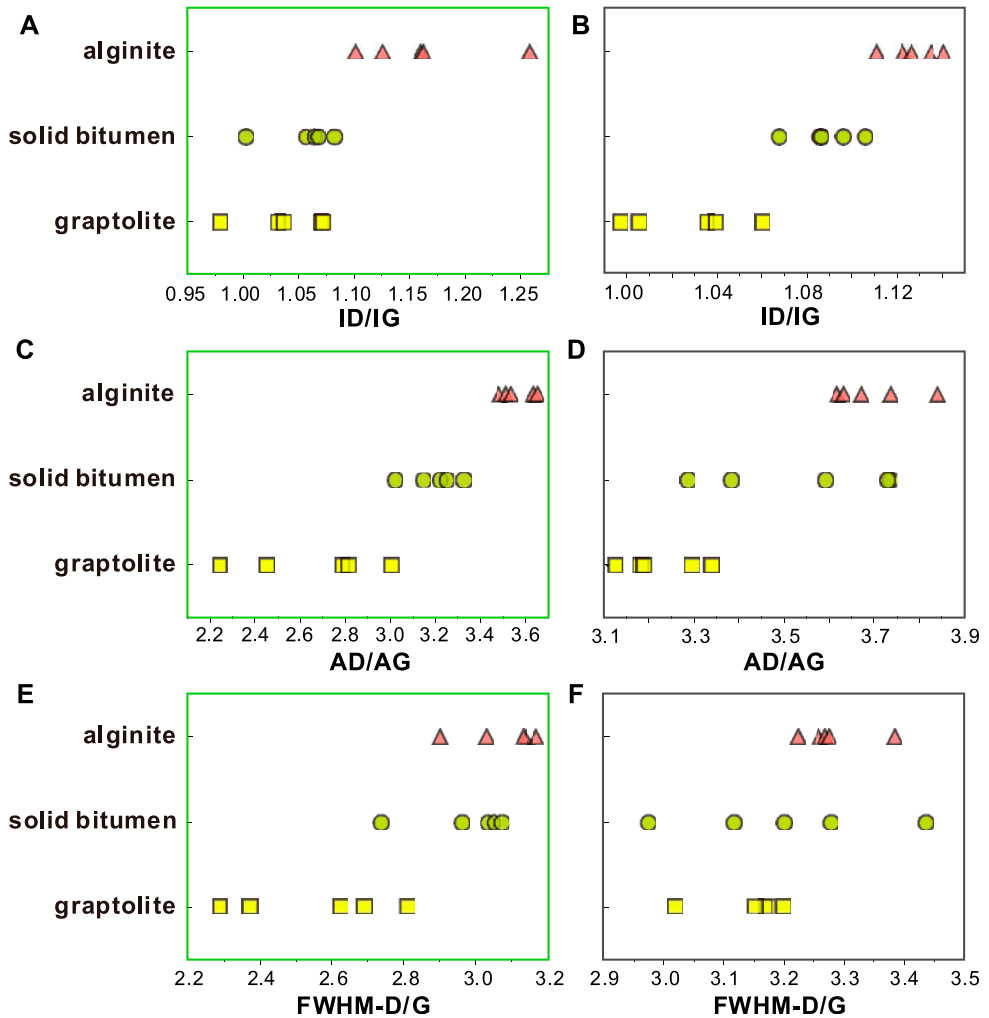

FIGURE 8 | Raman structural parameters of three macerals in jy2 HF (left) and ys118 (right) samples.

solid bitumen. Hence, the values of AD/AG and ID/IG were smaller in graptolite.

2) ID/IG could tell very well between the alginite and solid bitumen (**Figures 8A–B**). The ID/IG is usually employed as a thermal maturity indicator. When bitumen reflectance (BRo) is smaller than 3, ID/IG presents a negative correlation with BRo (Zhou et al., 2014). Furthermore, Ferralis et al. (2016) believed that an increase in thermal maturity would result in a decrease in the H/C atomic ratio. Therefore, we suggest that alginite has a greater ID/IG value than solid bitumen because of the greater hydrogen element content in the alginite.

However, AD/AG and FWHM-D/G are not thoroughly distinguished between alginite and solid bitumen (**Figure 8C–F**). This suggests that other factors may influence the maceral properties, and the possible reason is that solid bitumen forms in the many stages, e.g., in the immature, mature, and even over-mature stages (Misch et al., 2019). The different thermal evolution stages of the solid bitumen lead to different degrees of solid bitumen carbonization, resulting in a wide range for values of Raman structure parameters. Besides, in **Figure 3B**, it can be observed that part of the alginite is converted into solid bitumen, leading to a change of the structure from layered to non-layered. A similar alginite transformation process is also discovered by Liu et al. (2017). This process directly indicates that alginite and bitumen can form the mixtures so that they are not distinguishable by Raman spectral parameters. As a result, the ability of Raman spectral parameters for distinguishing solid bitumen and alginite is not good but still helps to some extent.

The Effect of Thermal Maturity on OM Pores

Table 1 and **Figure 5** show that the jy2 HF sample has a greater areal porosity and form factor than the ys118 sample. The reason might come from thermal maturity. Raman structure parameter analyses include G-D bands, AD/AG, FWHM-G, and FWHM-D/G in the alginite, solid bitumen, and graptolite. Excluding the G-D displacement difference parameter, the other three parameters in the jy2 HF sample have larger values compared

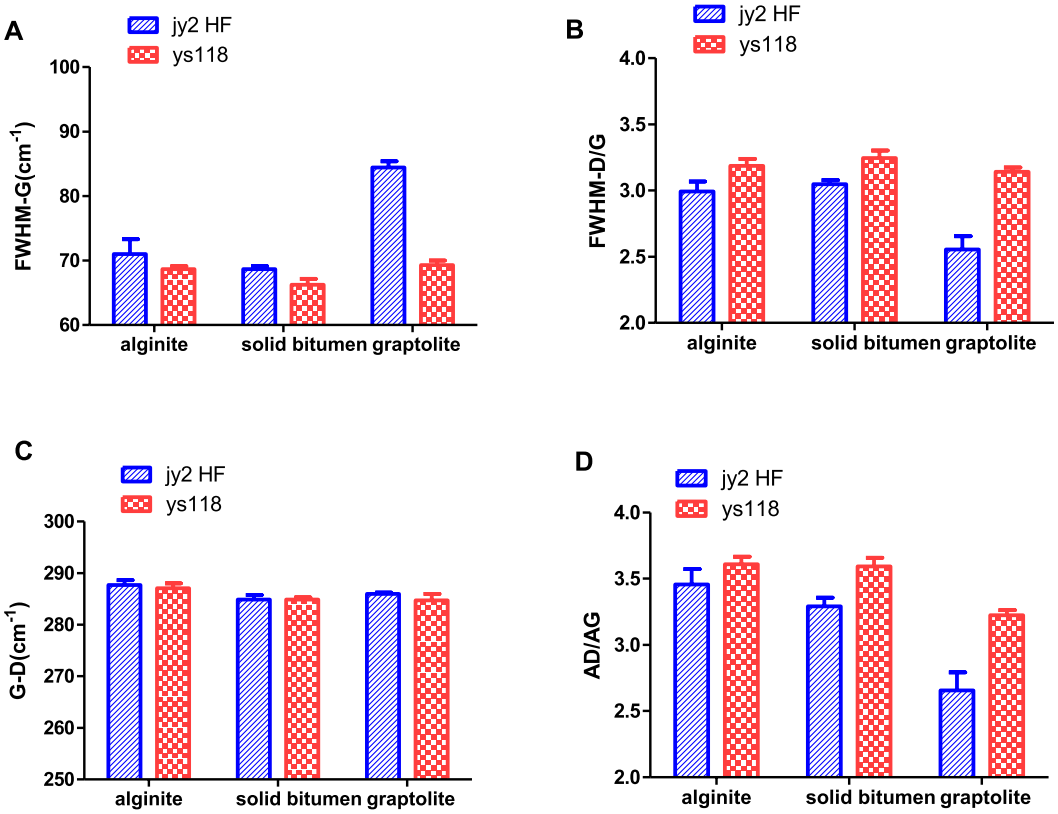

FIGURE 9 | Raman structural parameters of three macerals in different mature samples.

to those of the ys118 sample (**Figure 9**). The FWHM-G value of the jy118 sample is smaller than the ys2 HF sample since it is negatively correlated with thermal maturation (Maslova et al., 2012; Romero-Sarmiento et al., 2014).

FWHM-D/G and AD1/AG are positively correlated with thermal maturity (Zhou et al., 2014). Thus, the ys118 sample has a higher thermal maturity than the jy2 HF sample. Some researchers suggest a critical value of Ro around 2.5% (Wang et al., 2016; Yang et al., 2016; Chen et al., 2017). When Ro is greater than 2.5%, the organic porosity decreases (Wang et al., 2016). In this study, the ys118 sample has a higher thermal maturity but a smaller porosity. The reason may be attributed to the Ro of more than 2.5%.

Although thermal maturity may be one of the most important controlling factors for pore structure in organic matters, as discussed above, other factors should also be focused on, such compacted, the depth of buried shale, and coefficient (Jiao et al., 2017; Liu et al., 2019). The pressure coefficient of well ys118 (1.65 by Wang et al., 2018) is higher than that of well jy2 HF (1.5 by Feng et al., 2018). It is expected that the areal porosity of OM in well ys118 is higher than that of well jy2 HF. However, the results of the areal porosity of the OM from well jy2 HF did not follow the law that OM porosity is higher at greater pressure (**Table 1**). Thus, the pressure coefficient might be an alternative factor that has an impaction on the development of organic pores.

Compaction related to burial depth also compresses the pores to reduce the pore sizes and change the pore shapes from round or elliptical-shaped to slit-shaped (Jiao et al., 2017). When the depth of buried shale exceed 5,000 m, the pore structure occurs the obvious changes (Jiao et al., 2017). In this study, the difference of depth is blowing 5,000 m and only about 340 m. Therefore, compaction has little impaction on the development of organic pores.

CONCLUSION

The following conclusions are drawn from this study:

1) Three macerals are identified in the Longmaxi Formation, including the alginite, solid bitumen, and graptolite. The alginite and graptolite can be distinguished by the parameters of AD/AG and ID/IG.
2) The areal porosity of alginite is higher than the pyrobitumen, and a lower areal porosity is found in graptolite.
3) Under the condition of high-over thermal maturity, Raman spectroscopy is utilized to reflect the change of thermal maturity. AD1/AG and FWHM-D/G are positively correlated with thermal maturity, while FWHM-G is inversely correlated with thermal maturity. Therefore, thermal maturity should be responsible for the differences

in pore structure between the two shale gas fields (Chen et al., 2019a; Chen X. et al., 2019; Chen et al., 2020).

DATA AVAILABILITY STATEMENT

The original contributions presented in the study are included in the article/supplementary material. Further inquiries can be directed to the corresponding author.

AUTHOR CONTRIBUTIONS

QP contributed as the major author of the manuscript. GH conceived the project and analyzed the samples. CH and CZ collected the samples. All authors contributed to the article and approved the submitted version.

FUNDING

This study was jointly funded by the Key Laboratory of Unconventional Petroleum geology open fund project of CGS (2017) and by the National Natural Science Foundation of China (Grant Nos. 41872155 and U1663201).

ACKNOWLEDGMENTS

We are warmly grateful to Wang Jie and Ma Liangbang from Wuxi Research Institute of Petroleum Geology for their assistance with fieldwork. This study was jointly funded by the Key Laboratory of Unconventional Petroleum geology open fund project of CGS (2017) and by the National Natural Science Foundation of China (Grant Nos. 41872155 and U1663201).

REFERENCES

Bao, F., Li, Z. M., Zhang, M. Z., and Wang, R. C. (2012). Application of Laser Raman Spectrum in Organic Maceral Studies. *Pet. Geology. Exp.* 34 (1), 104–108. doi:10.11781/sysydz201201104 [In Chinese with English abstract].

Cardott, B. J., and Curtis, M. E. (2018). Identification and Nanoporosity of Macerals in Coal by Scanning Electron Microscopy. *Int. J. Coal Geology.* 190, 205–217. doi:10.1016/j.coal.2017.07.003

Chen, L., Jiang, Z., Liu, K., Tan, J., Gao, F., and Wang, P. (2017). Pore Structure Characterization for Organic-Rich Lower Silurian Shale in the Upper Yangtze Platform, South China: A Possible Mechanism for Pore Development. *J. Nat. Gas Sci. Eng.* 46, 1–15. doi:10.1016/j.jngse.2017.07.009

Chen, L., Jiang, Z., Liu, Q., Jiang, S., Liu, K., Tan, J., et al. (2019). Mechanism of Shale Gas Occurrence: Insights from Comparative Study on Pore Structures of marine and Lacustrine Shales. *Mar. Pet. Geology.* 104, 200–216. doi:10.1016/j.marpetgeo.2019.03.027

Chen, L., Liu, K., Jiang, S., Huang, H., Tan, J., and Zuo, L. (2021). Effect of Adsorbed Phase Density on the Correction of Methane Excess Adsorption to Absolute Adsorption in Shale. *Chem. Eng. J.* 420, 127678. doi:10.1016/j.cej.2020.127678

Chen, L., Lu, Y., Jiang, S., Li, J., Guo, T., and Luo, C. (2015). Heterogeneity of the Lower Silurian Longmaxi marine Shale in the Southeast Sichuan Basin of China. *Mar. Pet. Geology.* 65, 232–246. doi:10.1016/j.marpetgeo.2015.04.003

Chen, L., Zuo, L., Jiang, Z., Jiang, S., Liu, K., Tan, J., et al. (2019a). Mechanisms of Shale Gas Adsorption: Evidence from Thermodynamics and Kinetics Study of Methane Adsorption on Shale. *Chem. Eng. J.* 361, 559–570. doi:10.1016/j.cej.2018.11.185

Chen, X., Chen, L., Guo, X. S., and Wang, C. (2019b). Geochemical Characteristics of Shale Gas in the Silurian Longmaxi Formation, Jiaoshiba Area, Southeast Sichuan Basin, China. *Energy Fuels* 33, 8045–8054. doi:10.1021/acs.energyfuels.9b01305

Dai, J., Zou, C., Liao, S., Dong, D., Ni, Y., Huang, J., et al. (2014). Geochemistry of the Extremely High thermal Maturity Longmaxi Shale Gas, Southern Sichuan Basin. *Org. Geochem.* 74, 3–12. doi:10.1016/j.orggeochem.2014.01.018

Feng, W., Wang, F., Guan, J., Zhou, J., Wei, F., Dong, W., et al. (2018). Geologic Structure Controls on Initial Productions of Lower Silurian Longmaxi Shale in south China. *Mar. Pet. Geology.* 91, 163–178. doi:10.1016/j.marpetgeo.2018.01.001

Ferralis, N., Matys, E. D., Knoll, A. H., Hallmann, C., and Summons, R. E. (2016). Rapid, Direct and Non-destructive Assessment of Fossil Organic Matter via microRaman Spectroscopy. *Carbon* 108, 440–449. doi:10.1016/j.carbon.2016.07.039

Ferrari, A. C., and Robertson, J. (2000). Interpretation of Raman Spectra of Disordered and Amorphous Carbon. *Phys. Rev. B* 61 (20), 14095–14107. doi:10.1103/PhysRevB.61.14095

Fishman, N. S., Hackley, P. C., Lowers, H. A., Hill, R. J., Egenhoff, S. O., Eberl, D. D., et al. (2012). The Nature of Porosity in Organic-Rich Mudstones of the Upper Jurassic Kimmeridge clay Formation, north Sea, Offshore United Kingdom. *Int. J. Coal Geology.* 103, 32–50. doi:10.1016/j.coal.2012.07.012

Guan, Q., Lü, X., Dong, D., and Cai, X. (2019). Origin and Significance of Organic-Matter Pores in Upper Ordovician Wufeng-Lower Silurian Longmaxi Mudstones, Sichuan Basin. *J. Pet. Sci. Eng.* 176, 554–561. doi:10.1016/j.petrol.2019.01.079

Guedes, A., Valentim, B., Prieto, A. C., and Noronha, F. (2012). Raman Spectroscopy of Coal Macerals and Fluidized Bed Char Morphotypes. *Fuel* 97, 443–449. doi:10.1016/j.fuel.2012.02.05

Guedes, A., Valentim, B., Prieto, A. C., Rodrigues, S., and Noronha, F. (2010). Micro-Raman Spectroscopy of Collotelinite, Fusinite and Macrinite. *Int. J. Coal Geology.* 83 (4), 415–422. doi:10.1016/j.coal.2010.06.002

Guo, H., He, R., Jia, W., Peng, P. a., Lei, Y., Luo, X., et al. (2018). Pore Characteristics of Lacustrine Shale within the Oil Window in the Upper Triassic Yanchang Formation, southeastern Ordos Basin, China. *Mar. Pet. Geology.* 91, 279–296. doi:10.1016/j.marpetgeo.2018.01.013

Hackley, P. C., Valentine, B. J., Voortman, L. M., Van Oosten Slingeland, D. S. B., and Hatcherian, J. (2017). Utilization of Integrated Correlative Light and Electron Microscopy (iCLEM) for Imaging Sedimentary Organic Matter. *J. Microsc.* 267 (3), 371–383. doi:10.1111/jmi.12576

Hakimi, M. H., Abdullah, W. H., and Shalaby, M. R. (2012). Geochemical and Petrographic Characterization of Organic Matter in the Upper Jurassic Madbi Shale Succession (Masila Basin, Yemen): Origin, Type and Preservation. *Org. Geochem.* 49, 18–29. doi:10.1016/j.orggeochem.2012.05.005

Hinrichs, R., Brown, M. T., Vasconcellos, M. A. Z., Abrashev, M. V., and Kalkreuth, W. (2014). Simple Procedure for an Estimation of the Coal Rank Using Micro-raman Spectroscopy. *Int. J. Coal Geology.* 136, 52–58. doi:10.1016/j.coal.2014.10.013

Hu, G., Pang, Q., Jiao, K., Hu, C., and Liao, Z. (2020). Development of Organic Pores in the Longmaxi Formation Overmature Shales: Combined Effects of thermal Maturity and Organic Matter Composition. *Mar. Pet. Geology.* 116, 104314–14. doi:10.1016/j.marpetgeo.2020.104314

Hu, H., Hao, F., Lin, J., Lu, Y., Ma, Y., and Li, Q. (2017). Organic Matter-Hosted Pore System in the Wufeng-Longmaxi (O 3 W-S 1 1) Shale, Jiaoshiba Area, Eastern Sichuan Basin, China. *Int. J. Coal Geology.* 173, 40–50. doi:10.1016/j.coal.2017.02.004

Jehlička, J., Urban, O., and Pokorný, J. (2003). Raman Spectroscopy of Carbon and Solid Bitumens in Sedimentary and Metamorphic Rocks. *Spectrochimica Acta A: Mol. Biomol. Spectrosc.* 59 (10), 2341–2352. doi:10.1016/S1386-1425(03)00077-5

Jiao, K., Yao, S., Liu, C., Gao, Y., Wu, H., Li, M., et al. (2014). The Characterization and Quantitative Analysis of Nanopores in Unconventional Gas Reservoirs Utilizing FESEM-FIB and Image Processing: An Example from the Lower

Silurian Longmaxi Shale, Upper Yangtze Region, China. *Int. J. Coal Geology.* 128-129, 1–11. doi:10.1016/j.coal.2014.03.004

Jiao, K., Ye, Y., Liu, S., Ran, B., Deng, B., Li, Z., et al. (2017). Characterization and Evolution of Nanoporosity in Superdeeply Buried Shales: A Case Study of the Longmaxi and Qiongzhusi Shales from MS Well #1, North Sichuan Basin, China. *Energy Fuels* 32, 191–203. doi:10.1021/acs.energyfuels.7b02932

Kelemen, S. R., and Fang, H. L. (2001). Maturity Trends in Raman Spectra from Kerogen and Coal. *Energy Fuels* 15 (3), 653–658. doi:10.1021/ef0002039

Ko, L. T., Ruppel, S. C., Loucks, R. G., Hackley, P. C., Zhang, T., and Shao, D. (2018). Pore-types and Pore-Network Evolution in Upper Devonian-Lower Mississippian Woodford and Mississippian Barnett Mudstones: Insights from Laboratory thermal Maturation and Organic Petrology. *Int. J. Coal Geology.* 190, 3–28. doi:10.1016/j.coal.2017.10.001

Largeau, C., Derenne, S., Casadevall, E., Berkaloff, C., Corolleur, M., Lugardon, B., et al. (1990). Occurrence and Origin of "Ultralaminar" Structures in "Amorphous" Kerogens of Various Source Rocks and Oil Shales. *Org. Geochem.* 16, 889–895. doi:10.1016/0146-6380(90)90125-j

Liang, C., Jiang, Z., Zhang, C., Guo, L., Yang, Y., and Li, J. (2014). The Shale Characteristics and Shale Gas Exploration Prospects of the Lower Silurian Longmaxi Shale, Sichuan Basin, South China. *J. Nat. Gas Sci. Eng.* 21, 636–648. doi:10.1016/j.jngse.2014.09.034

Liu, B., Schieber, J., and Mastalerz, M. (2017). Combined SEM and Reflected Light Petrography of Organic Matter in the New Albany Shale (Devonian-Mississippian) in the Illinois Basin: A Perspective on Organic Pore Development with thermal Maturation. *Int. J. Coal Geology.* 184, 57–72. doi:10.1016/j.coal.2017.11.002

Liu, R., Hao, F., Engelder, T., Shu, Z., Yi, J., Xu, S., et al. (2019). Stress Memory Extracted from Shale in the Vicinity of a Fault Zone: Implications for Shale-Gas Retention. *Mar. Pet. Geology.* 102, 340–349. doi:10.1016/j.marpetgeo.2018.12.047

Liu, R., Hao, F., Engelder, T., Zhu, Z., Yi, J., Xu, S., et al. (2020a). Influence of Tectonic Exhumation on Porosity of Wufeng-Longmaxi Shale in the Fuling Gas Field of the Eastern Sichuan Basin, China. *Bulletin* 104, 939–959. doi:10.1306/08161918071

Liu, R., Zheng, J., Hao, F., Nie, Z., Heng, D., Tan, X., et al. (2020b). Variation in Pore Systems with Tectonic Stress in the Overthrust Wufeng-Longmaxi Shale of the Southern Sichuan Basin, China. *J. Nat. Gas Sci. Eng.* 83, 103617. doi:10.1016/j.jngse.2020.103617

Liu, X., Song, D., He, X., Nie, B., Wang, Q., Sun, R., et al. (2018). Coal Macromolecular Structural Characteristic and its Influence on Coalbed Methane Adsorption. *Fuel* 222, 687–694. doi:10.1016/j.fuel.2018.03.015

Löhr, S. C., Baruch, E. T., Hall, P. A., and Kennedy, M. J. (2015). Is Organic Pore Development in Gas Shales Influenced by the Primary Porosity and Structure of Thermally Immature Organic Matter?. *Org. Geochem.* 87 (3), 119–132. doi:10.1016/j.orggeochem.2015.07.010

Loucks, R. G., Reed, R. M., Ruppel, S. C., and Jarvie, D. M. (2009). Morphology, Genesis, and Distribution of Nanometer-Scale Pores in Siliceous Mudstones of the Mississippian Barnett Shale. *J. Sediment. Res.* 79 (12), 848–861. doi:10.2110/jsr.2009.092

Luo, Q., Hao, J., Skovsted, C. B., Xu, Y., Liu, Y., Wu, J., et al. (2018). Optical Characteristics of Graptolite-Bearing Sediments and its Implication for thermal Maturity Assessment. *Int. J. Coal Geology.* 195, 386–401. doi:10.1016/j.coal.2018.06.019

Luo, Q., Zhong, N., Dai, N., and Zhang, W. (2016). Graptolite-derived Organic Matter in the Wufeng-Longmaxi Formations (Upper Ordovician-Lower Silurian) of southeastern Chongqing, China: Implications for Gas Shale Evaluation. *Int. J. Coal Geology.* 153, 87–98. doi:10.1016/j.coal.2015.11.014

Ma, S. M., Zou, X. Y., Yan, M., Li, X. Q., and Zhao, P. (2015). Study on Relationship between Graptolite and Shale Gas Origin of Longmaxi Formation in Southern Sichuan. *Coal Sci. Tech.* 43 (4), 106–109. doi:10.13199/j.cnki.cst.2015.04.025 [In Chinese with English abstract].

Ma, Y., Zhong, N., Cheng, L., Pan, Z., Dai, N., Zhang, Y., et al. (2016). Pore Structure of the Graptolite-Derived OM in the Longmaxi Shale, southeastern Upper Yangtze Region, China. *Mar. Pet. Geology.* 72, 1–11. doi:10.1016/j.marpetgeo.2016.01.009

Maslova, O. A., Ammar, M. R., Guimbretière, G., Rouzaud, J.-N., and Simon, P. (2012). Determination of Crystallite Size in Polished Graphitized Carbon by Raman Spectroscopy. *Phys. Rev. B* 86 (13), 1–5. doi:10.1103/PhysRevB.86.134205

Mastalerz, M., Schimmelmann, A., Drobniak, A., and Chen, Y. (2013). Porosity of Devonian and Mississippian New Albany Shale across a Maturation Gradient: Insights from Organic Petrology, Gas Adsorption, and Mercury Intrusion. *Bulletin* 97 (10), 1621–1643. doi:10.1306/04011312194

Mastik, V., and Tinn, O. (2017). Leveilleites Hartnageli Foerste, 1923 (Rhodophyta?) from the Ordovician of Laurentia and Silurian of Baltica: Redescription and Designation of a Neotype. *Palaeoworld* 26 (4), 602–611. doi:10.1016/j.palwor.2017.04.002

Misch, D., Gross, D., Hawranek, G., Horsfield, B., Klaver, J., Mendez-Martin, F., et al. (2019). Solid Bitumen in Shales: Petrographic Characteristics and Implications for Reservoir Characterization. *Int. J. Coal Geology.* 205, 14–31. doi:10.1016/j.coal.2019.02.012

Morga, R. (2011). Micro-Raman Spectroscopy of Carbonized Semifusinite and Fusinite. *Int. J. Coal Geology.* 87 (3-4), 253–267. doi:10.1016/j.coal.2011.06.016

Mumm, A. S., and İnan, S. (2016). Microscale Organic Maturity Determination of Graptolites Using Raman Spectroscopy. *Int. J. Coal Geology.* 162, 96–107. doi:10.1016/j.coal.2016.05.002

Nie, H., Jin, Z., and Zhang, J. (2018). Characteristics of Three Organic Matter Pore Types in the Wufeng-Longmaxi Shale of the Sichuan Basin, Southwest China. *Sci. Rep.* 8 (1), 1–11. doi:10.1038/s41598-018-25104-5

Pacton, M., Fiet, N., and Gorin, G. (2006). Revisiting Amorphous Organic Matter in Kimmeridgian Laminites: what Is the Role of the Vulcanization Process in the Amorphization of Organic Matter?. *Terra Nova* 18 (6), 380–387. doi:10.1111/j.1365-3121.2006.00702.x

Romero-Sarmiento, M.-F., Rouzaud, J.-N., Bernard, S., Deldicque, D., Thomas, M., and Littke, R. (2014). Evolution of Barnett Shale Organic Carbon Structure and Nanostructure with Increasing Maturation. *Org. Geochem.* 71, 7–16. doi:10.1016/j.orggeochem.2014.03.008

Shang, X., Moczydłowska, M., Liu, P., and Liu, L. (2018). Organic Composition and Diagenetic Mineralization of Microfossils in the Ediacaran Doushantuo Chert Nodule by Raman and Petrographic Analyses. *Precambrian Res.* 314, 145–159. doi:10.1016/j.precamres.2018.05.029

Sonibare, O. O., Haeger, T., and Foley, S. F. (2010). Structural Characterization of Nigerian Coals by X-ray Diffraction, Raman and FTIR Spectroscopy. *Energy* 35 (12), 5347–5353. doi:10.1016/j.energy.2010.07.025

Tenger, B., Shen, B. J., Yu, L. J., Yang, Y. F., Zhang, W. T., Tao, C., et al. (2017). Mechanisms of Shale Gas Generation and Accumulation in the Ordovician Wufeng-Longmaxi Formation, Sichuan Basin, SW China. *Pet. Exploration Develop.* 44 (1), 69–78. doi:10.1016/S1876-3804(17)30009-5 [In Chinese with English abstract].

Tinn, O., Mastik, V., Ainsaar, L., and Meidla, T. (2015). Kalania Pusilla, an Exceptionally Preserved Non-calcified Alga from the Lower Silurian (Aeronian, Llandovery) of Estonia. *Palaeoworld* 24 (1), 207–214. doi:10.1016/j.palwor.2014.12.001

Tuinstra, F., and Koenig, J. L. (1970). Raman Spectrum of Graphite. *J. Chem. Phys.* 53, 1126–1130. doi:10.1063/1.1674108

Wang, P., Jiang, Z., Chen, L., Yin, L., Li, Z., Zhang, C., et al. (2016). Pore Structure Characterization for the Longmaxi and Niutitang Shales in the Upper Yangtze Platform, South China: Evidence from Focused Ion Beam-He Ion Microscopy, Nano-Computerized Tomography and Gas Adsorption Analysis. *Mar. Pet. Geology* 77, 1323–1337. doi:10.1016/j.marpetgeo.2016.09.001

Wang, P. W., Zou, C. N., Li, X. J., Jiang, L. W., Mei, J., Zhang, Z., and Li, Q. F. (2018). Main geological controlling factors of shale gas enrichment and high yield in Zhaotong demonstration area. *Acta Petrolei Sinica* 39 (7), 744–753 [In Chinese with English abstract].

Wang, Y., Dong, D., Li, X., Huang, J., Wang, S., and Wu, W. (2015). Stratigraphic sequence and sedimentary characteristics of Lower Silurian Longmaxi Formation in Sichuan Basin and its peripheral areas. *Natural Gas Industry B* 2 (2), 222–232. doi:10.1016/j.ngib.2015.07.014

Yang, F., Ning, Z., Wang, Q., Zhang, R., and Krooss, B. M. (2016). Pore structure characteristics of lower Silurian shales in the southern Sichuan Basin, China: Insights to pore development and gas storage mechanism. *Int. J. Coal Geology.* 156, 12–24. doi:10.1016/j.coal.2015.12.015

Zeng, P., and Guo, T. (2015). Enrichment of shale gas in different strata in Sichuan Basin and its periphery-The examples of the Cambrian Qiongzhusi Formation and the Silurian Longmaxi Formation. *Energy Explor. Exploit.* 33 (3), 277–298. doi:10.1260/0144-5987.33.3.277

Zhou, Q., Xiao, X., Pan, L., and Tian, H. (2014). The relationship between micro-Raman spectral parameters and reflectance of solid bitumen. *Int. J. Coal Geology*. 121, 19–25. doi:10.1016/j.coal.2013.10.013

Zhu, H., Ju, Y., Huang, C., Qi, Y., Ju, L., Yu, K., Li, W., Su, X., Feng, H., and Qiao, P. (2019). Tectonic and Thermal Controls on the Nano-Micro Structural Characteristic in a Cambrian Organic-Rich Shale. *Minerals* 9 (354), 354–20. doi:10.3390/min9060354

Zou, C. N., Zhao, Q., Dong, D. Z., Yang, Z., Qiu, Z., Liang, F., Wang, N., Huang, Y., Duan, A. X., Zhang, Q., and Hu, Z. M. (2017). Geological characteristics, main challenges and future prospect of shale gas. *Nat. Gas Geosci*. 2 (5-6), 273–288 [In Chinese with English abstract]. doi:10.1016/j.jnggs.2017.11.002

Zou, C. N., Dong, D. Z., Wang, S. J., Li, J. Z., Li, X. J., Wang, Y. M., et al. (2020). Geological Characteristics and Resource Potential of Shale Gas in China. *Pet. Exploration Develop*. 37, 641–653. doi:10.1016/S1876-3804(11)60001-3 [In Chinese with English abstract].

Conflict of Interest: The authors declare that the research was conducted in the absence of any commercial or financial relationships that could be construed as a potential conflict of interest.